Tropospheric ozone rise in the northern midlatitudes increasingly driven by nitrate particles.

Viral Shah[1,2]*, Christoph A. Keller[1,3], K. Emma Knowland[1,3], Amy Christiansen[4], Lu Hu[5], Haolin Wang[6], Xiao Lu[6], Becky Alexander[7], Daniel J. Jacob[8]

[1]Global Modeling and Assimilation Office (GMAO), NASA Goddard Space Flight Center, Greenbelt, MD 20770, USA
[2]Science Systems and Applications, Inc., Lanham, MD 20706, USA
[3]GESTAR II, Morgan State University, Baltimore, MD 21251, USA
[4]Division of Energy, Matter & Systems, University of Missouri-Kansas City, Kansas City, MO 64108, USA
[5]Department of Chemistry and Biochemistry, University of Montana, Missoula, MT 59812, USA
[6]School of Atmospheric Sciences, Sun Yat-sen University, Zhuhai, Guangdong, 519082, P.R. China
[7]Department of Atmospheric Sciences, University of Washington, Seattle, WA 98195, USA
[8]Harvard John A. Paulson School of Engineering and Applied Sciences, Harvard University, Cambridge, MA 02138, USA

*Corresponding author: Viral Shah
Email: viral.shah@nasa.gov

Abstract

Tropospheric ozone is a major air pollutant and greenhouse gas whose anthropogenic production is limited principally by the supply of nitrogen oxides (NO_x) from combustion. The background ozone concentration in the extratropical northern hemisphere has been increasing at 5% per decade since the 1950s, a trend that has continued into the 21st century despite the leveling off of NO_x emissions. Here we explain this sustained increase by the photolysis of nitrate aerosol particles (pNO_3^-) to regenerate NO_x. pNO_3^- forms from thermodynamic gas-aerosol partitioning of nitric acid, a product of NO_x oxidation, at low aerosol acidity. Including pNO_3^- photolysis in the GEOS-Chem global atmospheric chemistry model increases ozone in the extratropical northern hemisphere by up to 10 ppbv, improving the consistency with observations from ozonesondes and aircraft. pNO_3^- concentrations in the northern extratropics have likely been increasing over the past several decades because of decreasing aerosol acidity driven by falling anthropogenic SO_2 and rising anthropogenic ammonia emissions. We find in the model that this has augmented the increase in ozone in the northern extratropics by about 50% to better match the observed ozone trend. pNO_3^- is likely to continue to increase through 2050 and drive an increase in ozone. Further work is needed to better determine the rates and mechanism of pNO_3^- photolysis.

Significance statement

Tropospheric ozone is a major greenhouse gas whose concentrations have been rising in the northern midlatitudes in the past three decades despite flattening emissions of nitrogen oxides, its main precursor. We find that this ozone growth is increasingly caused by the photolysis of nitrate particles to regenerate nitrogen oxides, combined with an increasing trend of nitrate particles due to decreasing aerosol acidity from falling sulfur dioxide emissions and rising ammonia emissions. Our results point to the importance of reducing the uncertainty in the rates of the photolysis of nitrate particles and improving its representation in atmospheric chemistry models in order to make accurate future projections of climate forcing from tropospheric ozone.

Main Text

Introduction

Tropospheric ozone is a short-lived climate forcer and a highly reactive gas that can damage human cells and tissue and reduce plant productivity. It mostly forms from the oxidation of carbon monoxide (CO), methane, and volatile organic compounds in the presence of sufficient

amounts of nitrogen oxides ($NO_x \equiv NO+NO_2$). A smaller amount is transported from the stratosphere. Tropospheric ozone concentrations in the northern midlatitudes have risen by about 50% since the early 20th century because of rising anthropogenic emissions of ozone precursors (1). This trend has continued into the 21st century (2–4), although the rise in global precursor emissions has slowed down (5). Between the 1990s and 2017, ozone concentrations in the northern hemisphere increased by an average of 5% or 2 ppbv per decade in the free troposphere, the layer between ~2 km and the tropopause (3, 4). Ozone in the free troposphere has a larger effect on climate than ozone near the surface (6). Free tropospheric ozone also mixes down and contributes to ozone pollution at the surface (7, 8). However, global atmospheric chemistry models cannot account for the observed ozone increase (3, 4, 9, 10), implying that they are missing key processes. It is important to identify these processes to improve our ability to make accurate future projections of climate forcing and air pollution from tropospheric ozone.

Tropospheric ozone has long been a focus of global atmospheric chemistry modeling, but there are major differences between models in global production and loss rates (11–14). Notably, only a few models include tropospheric halogen chemistry, an important sink for ozone and NO_x (15–17). When included in the widely used GEOS-Chem model, halogen chemistry lowers the tropospheric ozone burden by 15% (17). At the same time, many models, including GEOS-Chem, underestimate ozone production over the tropical oceans because of an underestimate in NO_x concentrations (18, 19).

The photolysis of nitrate particles (pNO_3^-) has been proposed as a major route for recycling NO_x over the oceans (20–23). pNO_3^- is produced by the gas-particle partitioning of nitric acid (HNO_3), the dominant sink of NO_x, at low temperature, high humidity, and low aerosol acidity, associated with high ammonia, low sulfate, and freshly emitted sea salt aerosols. Photolysis of nitrate ions in aqueous solutions produces nitrous acid (HONO) and NO_2, which volatilize to the gas phase (24):

$$NO_3^- + h\nu \xrightarrow{H_2O\,(l)} HONO(g) + OH^- + O(^3P) \quad \text{(R1a)}$$

$$\xrightarrow{H_2O\,(l)} NO_2(g) + OH^- + OH \quad \text{(R1b)}$$

Using aircraft-based HONO observations over the oceans, studies have inferred a pNO_3^- photolysis frequency on the order of 10^{-4} s^{-1}, which is about 2 orders of magnitude faster than the photolysis frequency of gas-phase HNO_3 (20, 23). These faster rates are supported by

laboratory studies on ambient pNO_3^- (25–27). Some field and laboratory studies suggest that the reaction is too slow ($<10^{-5}$ s^{-1}) to be a significant path for recycling NO_x (28–30). However, Shah et al. (31) showed that including this reaction in the GEOS-Chem model at rates within the range of current estimates corrects the NO_x underestimate over the oceans and increases the production of tropospheric ozone in the model.

Here we show that including the parameterization of pNO_3^- photolysis from Shah et al. (31) improves the ability of the GEOS-Chem model to simulate the observed tropospheric ozone distribution as well as the trends in the northern midlatitudes since the mid-1990s. Further simulations indicate that increasing pNO_3^- concentrations has augmented the growth in tropospheric ozone over the northern midlatitudes since the middle of the 20th century and could continue to do so until the middle of the 21st century.

Results and Discussion

Tropospheric ozone distribution in 2018

We begin by evaluating the GEOS-Chem ozone simulation for the year 2018 using observations of ozone vertical profiles from the global ozonesonde network (32, 33), and the In-service Aircraft for a Global Observing System (IAGOS) program (34). Ozonesonde measurements are made using the electrochemical cell which has an accuracy of better than ±10% in much of the troposphere (1, 35). The IAGOS measurements are made using a dual-beam ultraviolet absorption photometer, with an accuracy of ±2 ppbv (36, 37). Comparisons between the two observations show the IAGOS measurements to be low relative to the ozonesonde measurements by 5–8% (1, 38). See *Materials and Methods* for further details. For our simulations, we use GEOS-Chem version 14.2.0 at a 4º latitude ×5º longitude resolution driven by meteorological reanalysis data from the NASA Global Modeling and Assimilation Office's (GMAO) Modern-Era Retrospective analysis for Research and Applications, Version 2 (MERRA-2) (39). This version of GEOS-Chem includes pNO_3^- photolysis following Shah et al. (31) and other updates to the ozone simulation as described in *Materials and Methods*. For comparison with the ozonesonde and IAGOS measurements, we sample the model at the measurement location and within a 3-hour window of the measurement time.

Figure 1 shows the annual mean ozone distribution in the middle troposphere (800–400 hPa or ~2–7 km altitude) from the ozonesonde and IAGOS observations and GEOS-Chem simulations in 2018. Figure 2 shows the observed and simulated ozone vertical profiles between the surface

and 200 hPa, and the seasonal variation of mid-tropospheric ozone concentrations over six regions. The global mean ozone concentration in the middle troposphere in the ensemble of ozonesonde and IAGOS observations is 47.4 ppbv. This is reproduced by GEOS-Chem with a mean bias of 2.8 ppbv, and within the observational uncertainty of ~8% implied by the bias between the ozonesonde and IAGOS measurements. The simulated ozone vertical profiles and seasonal variations also align with the observations in most regions (Fig. 2). The model overestimates ozone observations in the tropics, which could be from an overestimate in lightning NO_x emissions, the dominant source of free troposphere NO_x in the tropics. The global lightning NO_x emissions in GEOS-Chem is taken to be ~6 Tg N a^{-1}, but there is large uncertainty in this source with literature estimates ranging from 2 to 8 Tg N a^{-1} (40).

To test the effect of pNO_3^- photolysis on tropospheric ozone, we conduct a parallel simulation without this reaction. The ozone concentrations from this simulation are on average 2–6 ppbv lower than those in the base simulation, but they are still largely consistent with the observations within their uncertainty (Fig. 2). An exception is the northern extratropics in spring, where the effect of pNO_3^- photolysis is strongest, and excluding it introduces a negative bias of up to 10 ppbv compared to the observations over the Arctic, North America and Europe, and East Asia (bottom panel of Fig. 2). pNO_3^- concentrations are highest in spring because of efficient lifting to the free troposphere combined with relatively low temperatures and seasonally rising emissions of ammonia from agricultural sources. Actinic flux is also relatively high to enable pNO_3^- photolysis as well as ozone production. A low ozone bias in spring in the absence of pNO_3^- photolysis had been previously reported in recent versions of GEOS-Chem and attributed to halogen chemistry (3, 10, 17, 41). This bias is remedied by including pNO_3^- photolysis in the model, as also found by Colombi et al. (8) and Yang et al. (42) in comparison with ozonesonde and aircraft observations over South Korea in May–June 2016.

Multi-decadal trends in tropospheric ozone

Ozone concentrations in the free troposphere have increased by 1–6 ppbv $decade^{-1}$ in the northern hemisphere since the mid-1990s (3, 4, 10), but previous versions of GEOS-Chem could not capture that trend (3, 10). pNO_3^- concentrations in the northern midlatitudes have most likely increased over this period because of decreasing aerosol acidity due to decreasing sulfate and increasing ammonia (43, 44). Here, we examine the effect of rising pNO_3^- concentrations on ozone trends by conducting simulations for the year 1995. To isolate the effect of changing anthropogenic emissions, we switch only the fossil fuel emissions and methane levels to 1995

values, keeping the meteorology, biogenic, and fire emissions constant. Wang et al. (10) found these climatic factors to contribute little to the global ozone trend in GEOS-Chem between 1995 and 2018. We compare the simulated ozone changes to the observed ozone trends from the ozonesonde and IAGOS data calculated by Christiansen et al. (3) and Wang et al. (10).

Figure 3 compares the 1995 to 2018 change in mid-tropospheric ozone concentrations in the base GEOS-Chem simulation and the simulation without pNO_3^- photolysis to the observed trends. Both simulations show the fastest increase in tropospheric ozone over Asia, reflecting the increase in ozone precursor emissions in the region over this period (5, 45). However, the ozone increase in the base simulation is larger than that in the simulation without pNO_3^- photolysis, particularly in the northern midlatitudes. This is because pNO_3^- concentrations in the northern midlatitudes in the model doubled between 1995 and 2018. Over East Asia, the ozonesonde and IAGOS observations show mid-tropospheric ozone trends of 2.1–3.3 ppbv $decade^{-1}$. In comparison, the base GEOS-Chem simulation shows an increase of 2.3–2.7 ppbv $decade^{-1}$ at the measurement locations, but the simulation without pNO_3^- photolysis shows an increase of only 1.4–1.9 ppbv $decade^{-1}$, indicating that about a third of the increase in ozone over East Asia since the mid-1990s is driven by increasing pNO_3^-. The base simulation also reproduces the trend in the IAGOS data over North America better than the simulation without pNO_3^- photolysis, but it overestimates the IAGOS trend over Europe. The trends in the ozonesonde data over North America and Europe vary substantially, which suggests that they are strongly affected by meteorological variability (3).

The increase in pNO_3^- concentrations in the northern midlatitudes in the model between 1995 and 2018 is mainly caused by falling SO_2 emissions and rising ammonia emissions. According to the Community Emissions Data System (CEDS) (5), over this period global anthropogenic SO_2 emissions fell by 55% due to better emission controls and reduced use of coal for energy generation, while anthropogenic ammonia emissions rose by 20% due to increasing agricultural activity. pNO_3^- formation in the northern midlatitude free troposphere is limited by high aerosol acidity (46). Aerosol acidity drops when there is less sulfate and more ammonia, allowing more HNO_3 to condense as pNO_3^- (47). In addition, global aircraft NO_x emissions increased by 50% between 1995 and 2018 (48) and contributed to the increase in pNO_3^- in the free troposphere.

Emissions of SO_2, ammonia, and NO_x have changed considerably since the middle of the 20^{th} century and further changes are expected in the future (5, 49). We examined the effect of these

changes on long-term trends of pNO_3^- and ozone by simulating historical ozone levels for the years 1980 and 1960, and projected ozone levels for 2050. Again, we only consider changes in anthropogenic emissions and use constant (2018) meteorology, biogenic emissions, and fire emissions. Historical emissions are from CEDS (5), and future emissions from the SSP2-4.5 scenario (49) used in Phase 6 of the Coupled Model Intercomparison Project (CMIP6). SSP2-4.5 is a middle-of-the-road scenario in which future emissions largely follow the current trends (50).

Figure 4 shows the 1960–2050 change in mid-tropospheric ozone concentrations in the northern midlatitudes in the base GEOS-Chem simulation and the simulation without pNO_3^- photolysis. It also shows the change in total (anthropogenic and non-anthropogenic) global emissions of SO_2, NO_x and ammonia between 1960 and 2050. Throughout this period, ozone concentrations in the northern midlatitudes in the base simulation increase at a faster rate than in the simulation without pNO_3^- photolysis. The average rate of increase in the base simulation between 1960 and 2050 is 1.9 ppbv $decade^{-1}$ compared to 1.3 ppbv $decade^{-1}$ in the simulation without pNO_3^- photolysis. Free tropospheric ozone observations before the 1990s were too sparse and uncertain to be useful in evaluating these differences in the simulated trends (1). The effect of pNO_3^- on ozone trends in our simulations was smaller between 1960 and 1980 when SO_2 emissions were still rising, but it has been steadily increasing since then, because of increasing NO_x and ammonia emissions, and falling SO_2 emissions. Between 2018 and 2050, the base simulation shows ozone concentrations continuing to increase at the rate of 0.9 ppbv $decade^{-1}$ (under the SSP2-4.5 emissions scenario), despite a drop in NO_x emissions, being driven by trends in SO_2 and ammonia emissions. This result is not specific to the SSP2-4.5 scenario. Most SSP scenarios project a decrease in SO_2 emissions and increase in ammonia emissions between now and 2050, making it likely that increasing pNO_3^- will continue to raise tropospheric ozone concentrations in the northern midlatitudes.

Conclusions

Photolysis of nitrate particles (pNO_3^-) is generally not included in global atmospheric chemistry models but we show here that it improves the tropospheric ozone simulation in the GEOS-Chem model and can help account for the observed multi-decadal trends in ozone. pNO_3^- photolysis increases simulated free tropospheric ozone concentrations in the northern extratropics in the spring by up to 10 ppbv and counteracts the springtime ozone loss by halogen radicals that would otherwise cause a low bias in ozone in the model. We find that increasing pNO_3^-

concentrations due to falling global SO_2 emissions and rising global ammonia emissions since the 1980s have accelerated the increase in free tropospheric ozone over the northern midlatitudes and explain much of the observed growth in free tropospheric ozone over the region between 1995 and 2018. Increasing pNO_3^- will likely continue to raise ozone concentrations through 2050.

The significant effect of pNO_3^- photolysis on tropospheric ozone calls for further work to characterize its mechanism and rates. Here, we used a pNO_3^- photolysis frequency of 10–100 times that of HNO_3 depending on the aerosol composition (31), but there is high variability in this rate, with values ranging from 1 to 1000 times the HNO_3 photolysis frequency (20, 21, 23, 25, 26, 28–30, 51, 52). It is not clear what drives this variability, and this has bearing on our results, since the photolysis frequency of pNO_3^- determines how strongly pNO_3^- photolysis affects tropospheric ozone. These issues point to a need to better understand the factors that govern the rate of pNO_3^- photolysis and its effect on the distribution and tends of tropospheric ozone.

Materials and Methods

a. Ozone measurements

Ozonesondes: The ozonesonde global network provides observations of the vertical distribution of ozone between the surface and about 30 km at about 60 stations (32, 33). We use ozonesonde data from the following archives: Harmonization and Evaluation of Ground-based Instruments for Free Tropospheric Ozone Measurements group (HEGIFTOM v2) (accessed at https://hegiftom.meteo.be), NOAA Earth System Research Laboratory - Global Monitoring Division (53) (accessed at ftp://ftp.cmdl.noaa.gov/ozww/Ozonesonde/), the Southern Hemisphere ADditional OZonesondes (SHADOZ) (54–56) (accessed at https://tropo.gsfc.nasa.gov/shadoz/), and the World Ozone and Ultraviolet Data Center (WOUDC) (57) (doi:10.14287/10000008). The ozonesonde launch frequency varies among sites from once a month to thrice a week. We exclude stations with less than 2 profiles in a month and less than 8 months of observations. Table S1 lists the ozonesonde stations used in this work. We aggregate the observations at each site to monthly means.

IAGOS: The European Research Infrastructure IAGOS program provides ozone observations using commercial passenger aircraft (34). The IAGOS data is publicly available at the IAGOS data portal (doi: 10.25326/20) In this work, we only use the vertical profile observations from the take-off and landing portions of the flights, excluding observations from the cruise portion. We aggregate the profiles into 8 areas to account for the irregular sampling frequency at any one

airport, excluding areas with less than 2 profiles in a month and less than 8 months of observations (Table S2). We further aggregate the observations in each area to monthly means.

b. GEOS-Chem

We simulate tropospheric ozone using the GEOS-Chem atmospheric chemistry model (version 14.2.0; doi: 10.5281/zenodo.8411433) driven by meteorology from MERRA-2 reanalysis (39). GEOS-Chem includes a detailed representation of tropospheric and stratospheric gas and aerosol chemistry (16, 58–60), with recent updates to the tropospheric halogen chemistry (17), heterogeneous NO_x chemistry (61) and chemistry of several volatile organic compounds (62–64). Sea salt aerosol debromination was previously disabled in recent applications of the model, despite evidence that it takes place (65), because it caused excessive ozone depletion in the marine boundary layer (31). This was partly due to an error in how the titration of sea salt aerosol alkalinity was represented in the model. This error is now fixed, and we include sea salt aerosol debromination in our simulation. We also reduce the loss of ozone by iodine radicals by including the uptake of HOI, IONO, and $IONO_2$ on alkaline sea salt aerosols as I^- and by limiting the hydrolysis of $IONO_2$ to acidic aerosols. Ozone dry deposition in the model was recently updated to explicitly consider the reaction of ozone with sea surface I^- (66), and to use a higher surface resistance over snow and ice (67).

pNO_3^- photolysis in GEOS-Chem follows the original implementation of Kasibhatla et al. (22) with modifications from Shah et al. (31). The photolysis frequency of pNO_3^- is calculated by scaling the photolysis frequency of HNO_3 by an enhancement factor (EF). The EF is taken to be 100 for coarse mode pNO_3^- and between 10 and 100 for fine mode pNO_3^- depending on the fraction of pNO_3^- in sea salt aerosols (31):

$$\mathrm{EF} = \max\left(10, 100 \times \frac{1}{1+\frac{[\mathrm{pNO_3^-}]}{[\mathrm{SSA}]}}\right) \quad (1)$$

Here, $[\mathrm{pNO_3^-}]$ and [SSA] are the molar concentrations in air of fine mode pNO_3^- and sea salt aerosol. The molar concentration of sea salt is taken as $[\mathrm{SSA}] = 2.39\,[\mathrm{Na^+}]$ based on the fraction of Na^+ in seawater (68), and where Na^+ is the chemically inert sea salt aerosol species simulated by GEOS-Chem. The HONO:NO_2 yield is taken to be 2:1 (22). pNO_3^- forms from the condensation of HNO_3 to the particle phase. HNO_3 is produced from the oxidation of NO_x (69). The thermodynamic partitioning of HNO_3 to fine mode pNO_3^- is computed with ISORROPIA II (70, 71). Coarse mode pNO_3^- forms by the uptake of HNO_3 on sea salt aerosols (72). Uptake of HNO_3 on dust is not included here, though it is an option in GEOS-Chem (73). Photolysis frequencies in

the model are calculated using Fast-JX (58, 74). As described in Shah et al. (31), equation (1) fits the current ensemble of laboratory and field evidence for pNO_3^- photolysis, and it corrects previous GEOS-Chem low bias in simulating NO_x concentrations over the remote oceans.

Emissions are calculated by the Harmonized Emissions Component (HEMCO, version 3.0) (75, 76) and include anthropogenic emissions from the Community Emissions Data System (CEDS, April '21 release, doi:10.5281/zenodo.4074245) (5, 77), aircraft emissions from the Aviation Emissions Inventory Code (AEIC, v2.0) (48), fire emissions from the Global Fire Emissions Database (GFED4s) (78), biogenic emissions using Model of Emissions of Gases and Aerosols from Nature (MEGAN, v2.1) (79), and NO_x emissions from lightning (80) and soils (81). Table S3 lists the global NO_x, CO, and non-methane volatile organic compound emissions in our 2018 simulation. Methane concentrations are prescribed as surface boundary conditions based on the NOAA Global Monitoring Laboratory's flask measurements (82).

Our primary simulations are conducted for 2018 (with a spin-up period of six months). In addition, we conduct simulations for 4 other years (1960, 1980, 1995, and 2050) using year-specific anthropogenic emissions and methane concentrations but constant (2018) meteorology, biogenic emissions, and fire emissions. Historical anthropogenic emissions are taken from CEDS inventory and future emissions correspond to the CMIP6 SSP2-4.5 scenario. The CMIP6 emissions were implemented in HEMCO by Murray et al. (83). The AEIC inventory provides historical aircraft emissions from 1990 to 2019. For 1960 and 1980, we scale down the AEIC emissions based on the change in the aircraft emissions in the CEDS inventory with respect to 1990. Aircraft emissions for 2050 are from the CMIP6 SSP2-4.5 scenario. The NOAA measurements of surface methane concentrations are available for 1979–present. For 1960, we use the CMIP6 historical methane concentrations (84) and for 2050, projected methane concentrations for the SSP2-4.5 scenario (85). For each year, we conduct an additional simulation without pNO_3^- photolysis.

Table S4 shows the global tropospheric ozone budget in GEOS-Chem in 2018. It is represented in terms of the odd oxygen family (O_x; $O_x \equiv O_3+NO_2+\ldots$, see table for full definition) to account for rapid cycling among these species. Ozone constitutes 99% of tropospheric O_x. The tropospheric O_x burden in GEOS-Chem for 2018 is 361 Tg, slightly higher than the range of 324–345 Tg inferred from ozonesonde and satellite measurements for 2010–16 (86), but within the range of models evaluated in the Tropospheric Ozone Assessment Report (TOAR) (14) and CMIP6 ((87). pNO_3^- photolysis increases the O_x burden by 7%, because of a 12% increase in

chemical production of O_x to 5470 Tg a^{-1} on account of higher NO_x concentrations (31). The increase in O_x production in the model occurs largely over the oceans, where pNO_3^- photolysis has the largest effect on NO_x concentrations and the O_x production efficiency per unit NO_x is high.

The lifetime of O_x against chemical loss and deposition in our base simulation is 21.4 days (Table S4), which is lower than the TOAR and CMIP6 multi-model means. The models in these intercomparisons generally do not consider tropospheric halogen chemistry, which reduces O_x lifetime in GEOS-Chem by about 2 days (17). Many of the models also do not include pNO_3^- formation. Including pNO_3^- photolysis in GEOS-Chem decreases the O_x lifetime by 0.6 days, mostly because it increases tropospheric OH concentrations, although these are now likely overestimated in the model (31). pNO_3^- photolysis is also a direct sink of O_x through its HONO channel.

References

1. D. W. Tarasick, *et al.*, Tropospheric Ozone Assessment Report: Tropospheric ozone from 1877 to 2016, observed levels, trends and uncertainties. *Elementa: Science of the Anthropocene* **7**, 39 (2019).

2. J. R. Ziemke, *et al.*, Trends in global tropospheric ozone inferred from a composite record of TOMS/OMI/MLS/OMPS satellite measurements and the MERRA-2 GMI simulation. *Atmos. Chem. Phys.* **19**, 3257–3269 (2019).

3. A. E. Christiansen, L. J. Mickley, J. Liu, L. D. Oman, L. Hu, Multidecadal increases in global tropospheric ozone derived from ozonesonde and surface site observations: can models reproduce ozone trends? *Atmos. Chem. Phys.* **22**, 14751–14782 (2022).

4. A. Gaudel, *et al.*, Aircraft observations since the 1990s reveal increases of tropospheric ozone at multiple locations across the Northern Hemisphere. *Sci. Adv.* **6**, eaba8272 (2020).

5. R. M. Hoesly, *et al.*, Historical (1750–2014) anthropogenic emissions of reactive gases and aerosols from the Community Emissions Data System (CEDS). *Geosci. Model Dev.* **11**, 369–408 (2018).

6. A. A. Lacis, D. J. Wuebbles, J. A. Logan, Radiative forcing of climate by changes in the vertical distribution of ozone. *J. Geophys. Res.* **95**, 9971–9981 (1990).

7. M. Lin, L. W. Horowitz, R. Payton, A. M. Fiore, G. Tonnesen, US surface ozone trends and extremes from 1980 to 2014: quantifying the roles of rising Asian emissions, domestic controls, wildfires, and climate. *Atmos. Chem. Phys.* **17**, 2943–2970 (2017).

8. N. K. Colombi, *et al.*, Why is ozone in South Korea and the Seoul metropolitan area so high and increasing? *Atmos. Chem. Phys.* **23**, 4031–4044 (2023).

9. R. B. Skeie, *et al.*, Historical total ozone radiative forcing derived from CMIP6 simulations. *npj Clim Atmos Sci* **3**, 32 (2020).

10. H. Wang, *et al.*, Global tropospheric ozone trends, attributions, and radiative impacts in 1995–2017: an integrated analysis using aircraft (IAGOS) observations, ozonesonde, and multi-decadal chemical model simulations. *Atmos. Chem. Phys.* **22**, 13753–13782 (2022).

11. D. S. Stevenson, *et al.*, Multimodel ensemble simulations of present-day and near-future tropospheric ozone. *J. Geophys. Res.* **111**, D08301 (2006).

12. S. Wu, *et al.*, Why are there large differences between models in global budgets of tropospheric ozone? *J. Geophys. Res.* **112** (2007).

13. L. Hu, *et al.*, Global budget of tropospheric ozone: Evaluating recent model advances with satellite (OMI), aircraft (IAGOS), and ozonesonde observations. *Atmospheric Environment* **167**, 323–334 (2017).

14. P. J. Young, *et al.*, Tropospheric Ozone Assessment Report: Assessment of global-scale model performance for global and regional ozone distributions, variability, and trends. *Elementa: Science of the Anthropocene* **6**, 10 (2018).

15. A. Saiz-Lopez, *et al.*, Estimating the climate significance of halogen-driven ozone loss in the tropical marine troposphere. *Atmos. Chem. Phys.* **12**, 3939–3949 (2012).

16. T. Sherwen, *et al.*, Global impacts of tropospheric halogens (Cl, Br, I) on oxidants and composition in GEOS-Chem. *Atmos. Chem. Phys.* **16**, 12239–12271 (2016).

17. X. Wang, *et al.*, Global tropospheric halogen (Cl, Br, I) chemistry and its impact on oxidants. *Atmos. Chem. Phys.* **21**, 13973–13996 (2021).

18. H. Guo, *et al.*, Heterogeneity and chemical reactivity of the remote troposphere defined by aircraft measurements – corrected. *Atmos. Chem. Phys.* **23**, 99–117 (2023).

19. K. R. Travis, *et al.*, Constraining remote oxidation capacity with ATom observations. *Atmos. Chem. Phys.* **20**, 7753–7781 (2020).

20. C. Ye, *et al.*, Rapid cycling of reactive nitrogen in the marine boundary layer. *Nature* **532**, 489–491 (2016).

21. C. Reed, *et al.*, Evidence for renoxification in the tropical marine boundary layer. *Atmos. Chem. Phys.* **17**, 4081–4092 (2017).

22. P. Kasibhatla, *et al.*, Global impact of nitrate photolysis in sea-salt aerosol on NO_x, OH, and O_3; in the marine boundary layer. *Atmos. Chem. Phys.* **18**, 11185–11203 (2018).

23. S. T. Andersen, *et al.*, Extensive field evidence for the release of HONO from the photolysis of nitrate aerosols. *Sci. Adv.* **9**, eadd6266 (2023).

24. J. Mack, J. R. Bolton, Photochemistry of nitrite and nitrate in aqueous solution: a review. *J. Photochem. Photobiol., A* **128**, 1–13 (1999).

25. C. Ye, N. Zhang, H. Gao, X. Zhou, Photolysis of Particulate Nitrate as a Source of HONO and NO_x . *Environ. Sci. Technol.* **51**, 6849–6856 (2017).

26. F. Bao, M. Li, Y. Zhang, C. Chen, J. Zhao, Photochemical Aging of Beijing Urban $PM_{2.5}$: HONO Production. *Environ. Sci. Technol.* **52**, 6309–6316 (2018).

27. M. Gen, R. Zhang, D. D. Huang, Y. Li, C. K. Chan, Heterogeneous Oxidation of SO_2 in Sulfate Production during Nitrate Photolysis at 300 nm: Effect of pH, Relative Humidity, Irradiation Intensity, and the Presence of Organic Compounds. *Environ. Sci. Technol.* **53**, 8757–8766 (2019).

28. P. S. Romer, *et al.*, Constraints on Aerosol Nitrate Photolysis as a Potential Source of HONO and NO_x. *Environ. Sci. Technol.* **52**, 13738–13746 (2018).

29. Q. Shi, *et al.*, Laboratory Investigation of Renoxification from the Photolysis of Inorganic Particulate Nitrate. *Environ. Sci. Technol.* **55**, 854–861 (2021).

30. Y. Zhu, *et al.*, An investigation into the chemistry of HONO in the marine boundary layer at Tudor Hill Marine Atmospheric Observatory in Bermuda. *Atmos. Chem. Phys.* **22**, 6327–6346 (2022).

31. V. Shah, *et al.*, Nitrogen oxides in the free troposphere: implications for tropospheric oxidants and the interpretation of satellite NO_2 measurements. *Atmos. Chem. Phys.* **23**, 1227–1257 (2023).

32. D. W. Tarasick, *et al.*, Improving ECC Ozonesonde Data Quality: Assessment of Current Methods and Outstanding Issues. *Earth and Space Science* **8** (2021).

33. R. M. Stauffer, *et al.*, An Examination of the Recent Stability of Ozonesonde Global Network Data. *Earth and Space Science* **9**, e2022EA002459 (2022).

34. A. Petzold, *et al.*, Global-scale atmosphere monitoring by in-service aircraft – current achievements and future prospects of the European Research Infrastructure IAGOS. *Tellus B: Chem. Phys. Meteorol.* **67**, 28452 (2015).

35. A. M. Thompson, *et al.*, Ozonesonde Quality Assurance: The JOSIE–SHADOZ (2017) Experience. *Bull. Amer. Meteor. Soc.* **100**, 155–171 (2019).

36. P. Nédélec, *et al.*, Instrumentation on commercial aircraft for monitoring the atmospheric composition on a global scale: the IAGOS system, technical overview of ozone and carbon monoxide measurements. *Tellus B: Chem. Phys. Meteorol.* **67**, 27791 (2015).

37. R. Blot, *et al.*, Internal consistency of the IAGOS ozone and carbon monoxide measurements for the last 25 years. *Atmos. Meas. Tech.* **14**, 3935–3951 (2021).

38. J. Staufer, *et al.*, Trajectory matching of ozonesondes and MOZAIC measurements in the UTLS – Part 2: Application to the global ozonesonde network. *Atmos. Meas. Tech.* **7**, 241–266 (2014).

39. R. Gelaro, *et al.*, The Modern-Era Retrospective Analysis for Research and Applications, Version 2 (MERRA-2). *J. Climate* **30**, 5419–5454 (2017).

40. U. Schumann, H. Huntrieser, The global lightning-induced nitrogen oxides source. *Atmos. Chem. Phys.* **7**, 3823–3907 (2007).

41. L. Zhu, *et al.*, Effect of Sea Salt Aerosol on Tropospheric Bromine Chemistry. *Atmos. Chem. Phys.* **19**, 6497–6507 (2019).

42. L. H. Yang, *et al.*, Tropospheric NO_2 vertical profiles over South Korea and their relation to oxidant chemistry: implications for geostationary satellite retrievals and the observation of NO_2 diurnal variation from space. *Atmos. Chem. Phys.* **23**, 2465–2481 (2023).

43. S. E. Bauer, *et al.*, Historical (1850–2014) Aerosol Evolution and Role on Climate Forcing Using the GISS ModelE2.1 Contribution to CMIP6. *J Adv Model Earth Syst* **12**, e2019MS001978 (2020).

44. F. Paulot, D. Paynter, P. Ginoux, V. Naik, L. W. Horowitz, Changes in the aerosol direct radiative forcing from 2001 to 2015: observational constraints and regional mechanisms. *Atmos. Chem. Phys.* **18**, 13265–13281 (2018).

45. J. Kurokawa, T. Ohara, Long-term historical trends in air pollutant emissions in Asia: Regional Emission inventory in ASia (REAS) version 3. *Atmos. Chem. Phys.* **20**, 12761–12793 (2020).

46. B. A. Nault, *et al.*, Chemical transport models often underestimate inorganic aerosol acidity in remote regions of the atmosphere. *Commun Earth Environ* **2**, 93 (2021).

47. H. Guo, *et al.*, Fine particle pH and the partitioning of nitric acid during winter in the northeastern United States. *J. Geophys. Res. Atmos.* **121**, 10,355-10,376 (2016).

48. N. W. Simone, M. E. J. Stettler, S. R. H. Barrett, Rapid estimation of global civil aviation emissions with uncertainty quantification. *Transp Res D Transp* **25**, 33–41 (2013).

49. M. J. Gidden, *et al.*, Global emissions pathways under different socioeconomic scenarios for use in CMIP6: a dataset of harmonized emissions trajectories through the end of the century. *Geosci. Model Dev.* **12**, 1443–1475 (2019).

50. O. Fricko, *et al.*, The marker quantification of the Shared Socioeconomic Pathway 2: A middle-of-the-road scenario for the 21st century. *Global Environmental Change* **42**, 251–267 (2017).

51. M. Gen, Z. Liang, R. Zhang, B. R. Go Mabato, C. K. Chan, Particulate nitrate photolysis in the atmosphere. *Environ. Sci.: Atmos.*, 10.1039.D1EA00087J (2022).

52. C. Ye, D. E. Heard, L. K. Whalley, Evaluation of Novel Routes for NO_x Formation in Remote Regions. *Environ. Sci. Technol.* **51**, 7442–7449 (2017).

53. C. W. Sterling, *et al.*, Homogenizing and estimating the uncertainty in NOAA's long-term vertical ozone profile records measured with the electrochemical concentration cell ozonesonde. *Atmos. Meas. Tech.* **11**, 3661–3687 (2018).

54. A. M. Thompson, *et al.*, First Reprocessing of Southern Hemisphere Additional Ozonesondes (SHADOZ) Ozone Profiles (1998–2016): 2. Comparisons With Satellites and Ground-Based Instruments. *J. Geophys. Res. Atmos.* **122** (2017).

55. J. C. Witte, *et al.*, First reprocessing of Southern Hemisphere ADditional OZonesondes (SHADOZ) profile records (1998–2015): 1. Methodology and evaluation. *J. Geophys. Res. Atmos.* **122**, 6611–6636 (2017).

56. J. C. Witte, *et al.*, First Reprocessing of Southern Hemisphere ADditional OZonesondes Profile Records: 3. Uncertainty in Ozone Profile and Total Column. *JGR Atmospheres* **123**, 3243–3268 (2018).

57. WOUDC Ozone Monitoring Community, World Meteorological Organization-Global Atmosphere Watch Program (WMO-GAW), World Ozone And Ultraviolet Radiation Data Centre (WOUDC), Ozone (2015) https:/doi.org/10.14287/10000001 (October 17, 2023).

58. S. D. Eastham, D. K. Weisenstein, S. R. H. Barrett, Development and Evaluation of the Unified Tropospheric–Stratospheric Chemistry Extension (UCX) for the Global Chemistry-Transport Model GEOS-Chem. *Atmos. Environ.* **89**, 52–63 (2014).

59. K. R. Travis, *et al.*, Why do models overestimate surface ozone in the Southeast United States? *Atmos. Chem. Phys.* **16**, 13561–13577 (2016).

60. C. Y. Gao, C. L. Heald, J. M. Katich, G. Luo, F. Yu, Remote Aerosol Simulated During the Atmospheric Tomography (ATom) Campaign and Implications for Aerosol Lifetime. *J. Geophys. Res. Atmos.* **127** (2022).

61. C. D. Holmes, *et al.*, The Role of Clouds in the Tropospheric NO_x Cycle: A New Modeling Approach for Cloud Chemistry and Its Global Implications. *Geophys. Res. Lett.* **46**, 4980–4990 (2019).

62. K. H. Bates, D. J. Jacob, A new model mechanism for atmospheric oxidation of isoprene: global effects on oxidants, nitrogen oxides, organic products, and secondary organic aerosol. *Atmos. Chem. Phys.* **19**, 9613–9640 (2019).

63. K. H. Bates, *et al.*, Development and evaluation of a new compact mechanism for aromatic oxidation in atmospheric models. *Atmos. Chem. Phys.* **21**, 18351–18374 (2021).

64. H.-A. Kwon, *et al.*, Top-down estimates of anthropogenic VOC emissions in South Korea using formaldehyde vertical column densities from aircraft during the KORUS-AQ campaign. *Elementa: Science of the Anthropocene* **9**, 00109 (2021).

65. R. Sander, *et al.*, Inorganic bromine in the marine boundary layer: a critical review. *Atmos. Chem. Phys.* **3**, 1301–1336 (2003).

66. R. J. Pound, T. Sherwen, D. Helmig, L. J. Carpenter, M. J. Evans, Influences of oceanic ozone deposition on tropospheric photochemistry. *Atmos. Chem. Phys.* **20**, 4227–4239 (2020).

67. J. G. M. Barten, L. N. Ganzeveld, G.-J. Steeneveld, M. C. Krol, Role of oceanic ozone deposition in explaining temporal variability in surface ozone at High Arctic sites. *Atmos. Chem. Phys.* **21**, 10229–10248 (2021).

68. F. J. Millero, R. Feistel, D. G. Wright, T. J. McDougall, The composition of Standard Seawater and the definition of the Reference-Composition Salinity Scale. *Deep Sea Research Part I: Oceanographic Research Papers* **55**, 50–72 (2008).

69. B. Alexander, *et al.*, Global inorganic nitrate production mechanisms: comparison of a global model with nitrate isotope observations. *Atmos. Chem. Phys.* **20**, 3859–3877 (2020).

70. C. Fountoukis, A. Nenes, ISORROPIA II: a computationally efficient thermodynamic equilibrium model for K^+–Ca^{2+}–Mg^{2+}–NH_4^+–Na^+–SO_4^{2-}–NO_3^-–Cl^-–H_2O aerosols. *Atmos. Chem. Phys.* **7**, 4639–4659 (2007).

71. H. O. T. Pye, *et al.*, Effect of changes in climate and emissions on future sulfate-nitrate-ammonium aerosol levels in the United States. *J. Geophys. Res.* **114** (2009).

72. X. Wang, *et al.*, The role of chlorine in global tropospheric chemistry. *Atmos. Chem. Phys.* **19**, 3981–4003 (2019).

73. T. D. Fairlie, *et al.*, Impact of mineral dust on nitrate, sulfate, and ozone in transpacific Asian pollution plumes. *Atmos. Chem. Phys.* **10**, 3999–4012 (2010).

74. H. Bian, M. J. Prather, Fast-J2: Accurate Simulation of Stratospheric Photolysis in Global Chemical Models. *J. Atmos. Chem.* **41**, 281–296 (2002).

75. C. A. Keller, *et al.*, HEMCO v1.0: a versatile, ESMF-compliant component for calculating emissions in atmospheric models. *Geosci. Model Dev.* **7**, 1409–1417 (2014).

76. H. Lin, *et al.*, Harmonized Emissions Component (HEMCO) 3.0 as a versatile emissions component for atmospheric models: application in the GEOS-Chem, NASA GEOS, WRF-GC, CESM2, NOAA GEFS-Aerosol, and NOAA UFS models. *Geosci. Model Dev.* **14**, 5487–5506 (2021).

77. E. E. McDuffie, *et al.*, A global anthropogenic emission inventory of atmospheric pollutants from sector- and fuel-specific sources (1970–2017): an application of the Community Emissions Data System (CEDS). *Earth Syst. Sci. Data* **12**, 3413–3442 (2020).

78. L. Giglio, J. T. Randerson, G. R. van der Werf, Analysis of daily, monthly, and annual burned area using the fourth-generation global fire emissions database (GFED4). *J. Geophys. Res. Biogeo.* **118**, 317–328 (2013).

79. A. B. Guenther, *et al.*, The Model of Emissions of Gases and Aerosols from Nature version 2.1 (MEGAN2.1): an extended and updated framework for modeling biogenic emissions. *Geoscientific Model Development* **5**, 1471–1492 (2012).

80. L. T. Murray, D. J. Jacob, J. A. Logan, R. C. Hudman, W. J. Koshak, Optimized regional and interannual variability of lightning in a global chemical transport model constrained by LIS/OTD satellite data. *J. Geophys. Res. Atmos.* **117** (2012).

81. R. C. Hudman, *et al.*, Steps towards a mechanistic model of global soil nitric oxide emissions: implementation and space based-constraints. *Atmos. Chem. Phys.* **12**, 7779–7795 (2012).

82. L. T. Murray, Lightning NO x and Impacts on Air Quality. *Curr Pollution Rep* **2**, 115–133 (2016).

83. L. T. Murray, E. M. Leibensperger, C. Orbe, L. J. Mickley, M. Sulprizio, GCAP 2.0: a global 3-D chemical-transport model framework for past, present, and future climate scenarios. *Geosci. Model Dev.* **14**, 5789–5823 (2021).

84. M. Meinshausen, *et al.*, Historical greenhouse gas concentrations for climate modelling (CMIP6). *Geosci. Model Dev.* **10**, 2057–2116 (2017).

85. M. Meinshausen, *et al.*, The shared socio-economic pathway (SSP) greenhouse gas concentrations and their extensions to 2500. *Geosci. Model Dev.* **13**, 3571–3605 (2020).

86. A. Gaudel, *et al.*, Tropospheric Ozone Assessment Report: Present-day distribution and trends of tropospheric ozone relevant to climate and global atmospheric chemistry model evaluation. *Elementa: Science of the Anthropocene* **6**, 39 (2018).

87. P. D. Griffiths, *et al.*, Tropospheric ozone in CMIP6 simulations. *Atmos. Chem. Phys.* **21**, 4187–4218 (2021).

Data and code: The measurements and model used in this study are publicly available. Ozone observations are available at https://hegiftom.meteo.be (HEGIFTOM), ftp://ftp.cmdl.noaa.gov/ozww/Ozonesonde/ (NOAA), https://tropo.gsfc.nasa.gov/shadoz/ (SHADOZ), doi:10.14287/10000008 (WOUDC), and https://iagos.aeris-data.fr/ (IAGOS). The GEOS-Chem source code is available at doi:10.5281/zenodo.8411433.

Acknowledgements: Work at the GMAO was supported by the NASA Satellite Needs Working Group (SNWG). Work at Harvard was supported by the Harvard–NUIST Joint Laboratory for Air Quality and Climate, the Samsung PM2.5 Strategic Research Program, and the US EPA Science to Achieve Results (STAR) program. A.C. and L.H. acknowledge additional support from NOAA (grants: NA19OAR4310174 and NA19OAR4310176). B.A. acknowledges funding from NSF (grant: AGS 2109323). We thank N. Colombi (Harvard), R.M. Stauffer, A.M. Thompson (NASA GSFC), M.J. Evans (University of York) and B.H. Henderson (US EPA) for helpful discussions. We are grateful to all contributors to the SHADOZ, NOAA GMD, WOUDC, and HEGIFTOM ozonesonde databases. MOZAIC/CARIBIC/IAGOS data were created with support from the European Commission, national agencies in Germany (BMBF), France (MESR), and the UK (NERC), and the IAGOS member institutions (https://www.iagos.org/organisation/). The participating airlines (Lufthansa, Air France, Austrian, China Airlines, Iberia, Cathay Pacific, Air Namibia, Sabena, Hawaiian airlines) supported IAGOS by carrying the measurement equipment free of charge since 1994. The data are available at http://www.iagos.org thanks to additional support from AERIS.

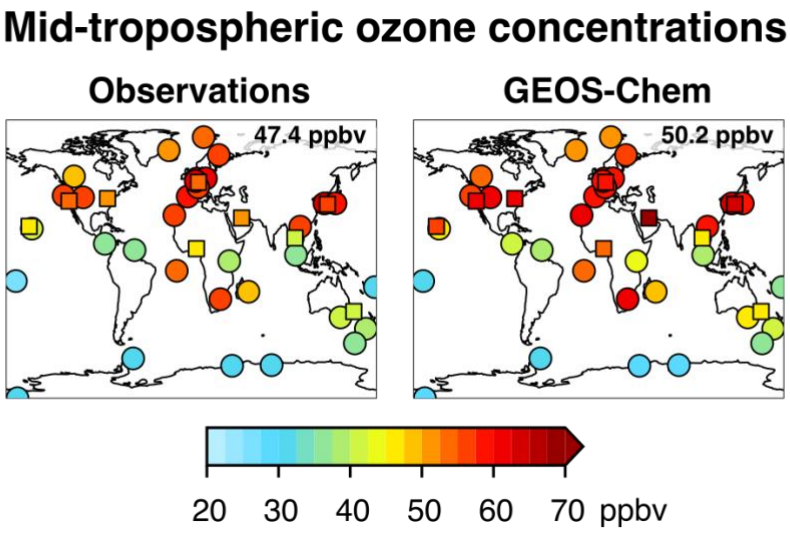

Figure 1. Annual mean ozone concentrations in the middle troposphere (800–400 hPa) in 2018. The left panel shows observed ozone concentrations from the ozonesonde (circles) and the IAGOS (squares) datasets (Tables S1 and S2). The right panel shows results from the GEOS-Chem simulation sampled at the measurement times and locations. The mean mid-tropospheric ozone concentrations from the observations and the model at the measurement sites are shown inset.

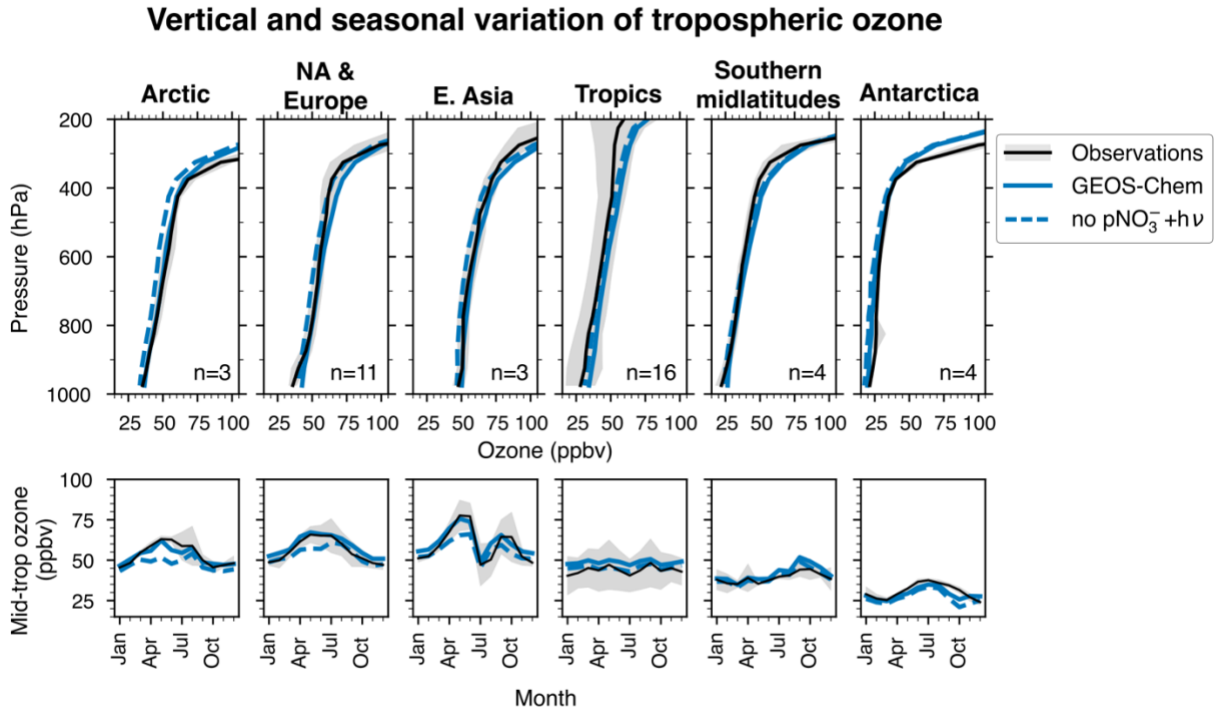

Figure 2. Vertical profiles and seasonal variations of tropospheric ozone over six regions in 2018. The top panels show the annual mean ozone concentrations between the surface and 200 hPa from the ozonesonde and IAGOS observations, and GEOS-Chem simulations aggregated into six regions. The bottom panels show the observed and simulated monthly mean ozone concentrations in the middle troposphere (800–400 hPa) over the six regions. The figure shows results from the base GEOS-Chem simulation (solid line) and from a simulation without pNO_3^- photolysis (dashed line). The number of sites (ozonesonde and IAGOS) in each region (n) is indicated in the top panels (Tables S1 and S2). The shaded areas denote ±1 standard deviation of the annual mean ozone profiles (top panel) and the monthly mid-tropospheric ozone concentrations (bottom panel) at the measurement sites in each region.

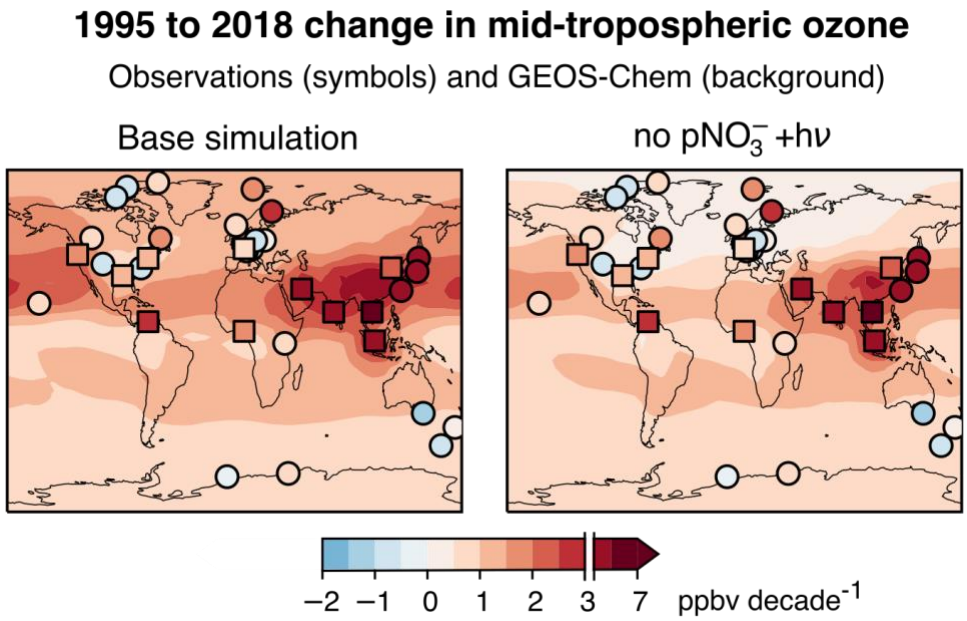

Figure 3. 1995 to 2018 emission-driven change in ozone concentrations in the middle troposphere. The top panels show the change of 800–400 hPa ozone concentrations in response to the change in anthropogenic emissions between 1995 and 2018 in the GEOS-Chem base simulation and a simulation without pNO_3^- photolysis. Also shown are the trends in mid-tropospheric ozone from ozonesonde (circles) and IAGOS (squares) observations as reported by Christiansen et al. (3) and Wang et al. (10), respectively. These trends were reported for 25 ozonesonde sites for 1990–2017 (1980–2017 for nine sites), and in 11 IAGOS areas for 1995–2017.

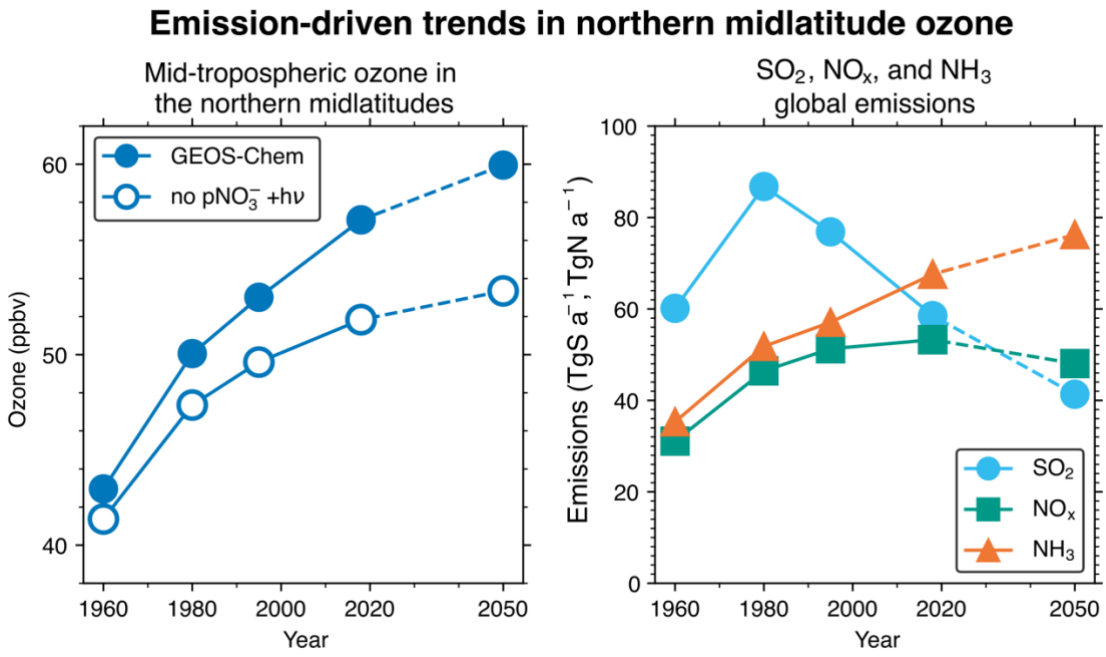

Figure 4. Emission-driven trends in tropospheric ozone concentrations at northern midlatitudes (30–60ºN) and global emissions of SO_2, NO_x, and NH_3. The left panel shows the mid-tropospheric (800–400 hPa mean) ozone concentrations from GEOS-Chem simulations using varying anthropogenic emissions (for years 1960, 1980, 1995, 2018, and 2050), but constant meteorology (year 2018). Historical anthropogenic emissions are from the Community Emissions Data System (5), and emissions for 2050 are from the SSP2-4.5 scenario (49) used in Phase 6 of the Coupled Model Intercomparison Project. GEOS-Chem results are shown for the base simulation and for the simulation without pNO_3^- photolysis. The right panel shows the annual emissions from all sources in GEOS-Chem.

Supplementary Information for
Tropospheric ozone rise in the northern midlatitudes increasingly driven by nitrate particles.

Viral Shah[1,2]*, Christoph A. Keller[1,3], K. Emma Knowland[1,3], Amy Christiansen[4], Lu Hu[5], Haolin Wang[6], Xiao Lu[6], Becky Alexander[7], Daniel J. Jacob[8]
[1]Global Modeling and Assimilation Office (GMAO), NASA Goddard Space Flight Center, Greenbelt, MD 20770, USA
[2]Science Systems and Applications, Inc., Lanham, MD 20706, USA
[3]GESTAR II, Morgan State University, Baltimore, MD 21251, USA
[4]Division of Energy, Matter & Systems, University of Missouri-Kansas City, Kansas City, MO 64108, USA
[5]Department of Chemistry and Biochemistry, University of Montana, Missoula, MT 59812, USA
[6]School of Atmospheric Sciences, Sun Yat-sen University, Zhuhai, Guangdong, 519082, P.R. China
[7]Department of Atmospheric Sciences, University of Washington, Seattle, WA 98195, USA
[8]Harvard John A. Paulson School of Engineering and Applied Sciences, Harvard University, Cambridge, MA 02138, USA

*Corresponding author: Viral Shah
Email: viral.shah@nasa.gov

This PDF file includes:
Tables S1 to S4

Table S1: Ozonesonde stations used for the evaluation of the 2018 simulations

Station	Latitude	Longitude	# of profiles [a]	Dataset[b]	Region
Ny-Ålesund	78.92°N	11.93°E	71	HEGIFTOM	Arctic
Scoresbysund	70.48°N	-21.97°W	52	HEGIFTOM	Arctic
Sodankyla	67.37°N	26.65°E	25	HEGIFTOM	Arctic
Edmonton	53.54°N	-114.1°E	35	HEGIFTOM	N. America
Lindenberg	52.21°N	14.12°E	62	WOUDC	Europe
De Bilt	52.1°N	5.18°E	54	HEGIFTOM	Europe
Uccle	50.8°N	4.35°E	142	HEGIFTOM	Europe
Payerne	46.49°N	6.57°E	133	WOUDC	Europe
Trinidad Head	40.8°N	124.2°W	49	NOAA	N. America
Madrid	40.47°N	3.68°W	51	HEGIFTOM	Europe
Boulder	40°N	105.3°W	50	NOAA	N. America
Tateno	36.06°N	140.1°E	46	WOUDC	E. Asia
Pohang	36.03°N	129.4°E	47	WOUDC	E. Asia
Izaña	28.3°N	16.48°W	35	HEGIFTOM	Tropics
Hanoi	21.01°N	105.8°E	30	SHADOZ	Tropics
Hilo	19.43°N	155.0°W	51	SHADOZ	Tropics
Costa Rica	9.94°N	84.04°W	34	SHADOZ	Tropics
Paramaribo	5.8°N	55.21°W	47	HEGIFTOM	Tropics
Kuala Lumpur	2.73°N	101.3°E	20	SHADOZ	Tropics
Nairobi	1.27°S	36.8°E	39	SHADOZ	Tropics
Ascension	7.58°S	14.24°W	43	SHADOZ	Tropics
Samoa	14.23°S	170.6°W	47	SHADOZ	Tropics
Fiji	18.13°S	178.4°E	41	SHADOZ	Tropics
Reunion	21.06°S	55.48°E	38	SHADOZ	Tropics
Irene	25.9°S	28.22°E	18	SHADOZ	Tropics
Broadmeadows	37.69°S	145.0 °E	48	WOUDC	Southern midlatitudes
Lauder	45°S	169.7°E	43	HEGIFTOM	Southern midlatitudes
Macquarie	54.5°S	159.0°E	51	WOUDC	Southern midlatitudes
Marambio	64.24°S	56.62°W	45	WOUDC	Antarctica
Davis	68.58°S	77.97°E	51	WOUDC	Antarctica
Syowa	69°S	39.58°E	51	WOUDC	Antarctica
South Pole	90°S	169°W	49	NOAA	Antarctica

a. Number of profiles in 2018.

b. HEGIFTOM: Harmonization and Evaluation of Ground-based Instruments for Free Tropospheric Ozone Measurements group; NOAA: NOAA Earth System Research Laboratory - Global Monitoring Division; SHADOZ: Southern Hemisphere ADditional Ozonesondes; WOUDC: World Ozone and Ultraviolet Data Center.

Table S2: IAGOS sites used for the evaluation of the 2018 simulations

Site	Latitude[a]	Longitude[a]	# of profiles[b]	Region
Western Europe	44–53°N	1°W – 14°E	312	Europe
Western US	32–48°N	105–123°W	207	N. America
Eastern US	28–45°N	71–97°W	53	N. America
China/Korea/Japan	26–43°N	113–142°E	232	E. Asia
Middle East	21–31°N	31–56°E	78	Tropics
Hawaii	19–22°N	156–158°W	279	Tropics
Central Africa	8°S–16°N	16°W–36°E	144	Tropics
Thailand	13.7°N	100.7°E	31	Tropics
Australia/New Zealand	27–43°S	144–175°E	46	Southern midlatitudes

a. Latitudinal and longitudinal range of the profiles aggregated at each site.

b. Number of profiles in 2018.

Table S3: Global NO_x, CO, and non-methane volatile organic compounds (VOC) emissions for 2018

Source	NO_x ($TgN\ a^{-1}$)	CO (Tg a-1)	Non-methane VOC (Tg C a-1)
Fuel combustion[a]	33.8	534	104
Aircraft[b]	1.1	1.2	0.1
Fires[c]	5.7	315	23.7
Biogenic[d]	4.5		601[e]
Lightning[f]	6.3		
Total	51.4	850	729

a. From the Community Emissions Data System (CEDS, April '21 release) (1, 2), except for ethane (3) and propane (4)
b. From the AEIC v2.0 inventory (5)
c. From GFEDv4.1s (6)
d. VOC emissions include terrestrial plant emissions from MEGAN v2.1 (7), emissions from plant decay (8), and oceanic sources (8, 9). Soil NO_x emissions are from (10).
e. Includes 302 Tg of isoprene emissions.
f. From Murray et al. (11).

Table S4: Global tropospheric ozone budget in GEOS-Chem and from model intercomparisons[a]

Model(s)	Burden (Tg)	Sources (Tg a^{-1})		Sinks (Tg a^{-1})		Lifetime (d)
		Chemical production	Strat-trop exchange[b]	Chemical loss	Deposition	
GEOS-Chem 14.2	361	5470	700	5070	1100[c]	21.4
No pNO_3^- photolysis[d]	338	4890	710	4580	1020[c]	22.0
TOAR[e]	340 ± 34	4937 ± 656	535 ± 161	4442 ± 570	996 ± 203	22.8[f]
CMIP6[g]	356 ± 31	4708 ± 589	277 ± 201	4122 ± 399	863 ± 40	25.5 ± 2.2

a. The budget is from the 2018 GEOS-Chem simulation and for the odd oxygen family ($O_x \equiv O_3 + NO_2 + HNO_3 + pNO_3^- + 2NO_3 + 3N_2O_5 + HNO_4$ + organic nitrates + $O(^1D)$ + XO + HOX + XNO_2 + $2XNO_3$ + $2Cl_2O_2$ + 2OClO + $2I_2O_2$ + 2OIO + $3I_2O_3$ + $4I_2O_4$; $X \equiv$ Cl, Br, I). The troposphere is defined as extending from the surface to model layer just below the one that contains the monthly mean thermal tropopause diagnosed form the GMAO MERRA-2 data.
b. Stratosphere-troposphere exchange, inferred as the difference between the total sinks and chemical production as the net change in ozone mass during the one-year simulation is negligible.
c. Deposition includes dry and wet deposition. Wet deposition is mainly as HNO_3.
d. GEOS-Chem simulation without pNO_3^- photolysis
e. From Young et al. (12). Values are for the year 2000. The intercomparison includes 49 models for the burden and about 33 models for the fluxes.
f. Calculated from the multimodel mean of the burden and sinks.
g. From Griffiths et al. (13) and summarized in Szopa et al. (14). Values are for the period 2005-14.

References

1. R. M. Hoesly, *et al.*, Historical (1750–2014) anthropogenic emissions of reactive gases and aerosols from the Community Emissions Data System (CEDS). *Geosci. Model Dev.* **11**, 369–408 (2018).

2. E. E. McDuffie, *et al.*, A global anthropogenic emission inventory of atmospheric pollutants from sector- and fuel-specific sources (1970–2017): an application of the Community Emissions Data System (CEDS). *Earth Syst. Sci. Data* **12**, 3413–3442 (2020).

3. Z. A. Tzompa-Sosa, *et al.*, Revisiting global fossil fuel and biofuel emissions of ethane. *JGR Atmospheres* **122**, 2493–2512 (2017).

4. Y. Xiao, *et al.*, Global budget of ethane and regional constraints on U.S. sources. *J. Geophys. Res.* **113**, D21306 (2008).

5. N. W. Simone, M. E. J. Stettler, S. R. H. Barrett, Rapid estimation of global civil aviation emissions with uncertainty quantification. *Transp Res D Transp* **25**, 33–41 (2013).

6. L. Giglio, J. T. Randerson, G. R. van der Werf, Analysis of daily, monthly, and annual burned area using the fourth-generation global fire emissions database (GFED4). *J. Geophys. Res. Biogeo.* **118**, 317–328 (2013).

7. A. B. Guenther, *et al.*, The Model of Emissions of Gases and Aerosols from Nature version 2.1 (MEGAN2.1): an extended and updated framework for modeling biogenic emissions. *Geoscientific Model Development* **5**, 1471–1492 (2012).

8. D. B. Millet, *et al.*, Global atmospheric budget of acetaldehyde: 3-D model analysis and constraints from in-situ and satellite observations. *Atmos. Chem. Phys.* **10**, 3405–3425 (2010).

9. J. A. Fisher, *et al.*, Methyl, Ethyl, and Propyl Nitrates: Global Distribution and Impacts on Reactive Nitrogen in Remote Marine Environments. *J. Geophys. Res. Atmos.* **123**, 12,429-12,451 (2018).

10. R. C. Hudman, *et al.*, Steps towards a mechanistic model of global soil nitric oxide emissions: implementation and space based-constraints. *Atmos. Chem. Phys.* **12**, 7779–7795 (2012).

11. L. T. Murray, D. J. Jacob, J. A. Logan, R. C. Hudman, W. J. Koshak, Optimized regional and interannual variability of lightning in a global chemical transport model constrained by LIS/OTD satellite data. *J. Geophys. Res. Atmos.* **117** (2012).

12. P. J. Young, *et al.*, Tropospheric Ozone Assessment Report: Assessment of global-scale model performance for global and regional ozone distributions, variability, and trends. *Elementa: Science of the Anthropocene* **6**, 10 (2018).

13. P. D. Griffiths, *et al.*, Tropospheric ozone in CMIP6 simulations. *Atmos. Chem. Phys.* **21**, 4187–4218 (2021).

14. S. Szopa, *et al.*, “Short-Lived Climate Forcers” in *Climate Change 2021: The Physical Science Basis. Contribution of Working Group I to the Sixth Assessment Report of the*

Intergovernmental Panel on Climate Change [Masson-Delmotte, V., P. Zhai, A. Pirani, S.L. Connors, C. Péan, S. Berger, N. Caud, Y. Chen, L. Goldfarb, M.I. Gomis, M. Huang, K. Leitzell, E. Lonnoy, J.B.R. Matthews, T.K. Maycock, T. Waterfield, O. Yelekçi, R. Yu, and B. Zhou (Eds.)], (Cambridge University Press, 2021), pp. 817–922.